Supplementary Materials for Robust quantum computational advantage with programmable 3050-photon Gaussian boson sampling

Contents

1 Squeezed light source **3**

1.1 Squeezed light generation . . . 3

1.2 Filtering of non-degenerate spectral modes . . . 5

1.3 Theoretical simulation of the joint spectral property of the squeezed light sources . 7

1.4 Measurement of the spectral purity . . . 9

1.5 Measured spectral purity under different squeezing level . . . 10

1.6 Measured spectral purity under different temporal delay . . . 11

2 Ultra-large programmable photonic circuit **13**

2.1 Spatial-temporal hybrid interference network . . . 13

2.2 Programmability of the system . . . 13

2.3 Phase stabilization of the circuit . . . 15

2.4 Fast feedback of seed laser frequency by referencing to an ultra low expansion (ULE) cavity . . . 17

3 Calibration of the transformation matrix **19**

3.1 Measurement of the matrix amplitude . . . 19

3.2 Measurement of the matrix phase . . . 21

3.2.1 Measurement of phase inside the circuit . . . 21

3.2.2 Determine the phase of the squeezed light sources . . . 24

3.2.3 Accuracy of phase stablization and calibration . . . 25

4 Multiple groups of experiments with different circuit depth and input scale **26**

5 Partial photon indistinguishability model **28**

6 Matrix product state method **29**

6.1 Decomposition of the output state of GBS . . . 29

6.1.1 Analytic method to decompose the output state . . . 30

6.2 Estimate the lower bound of required bond dimension size to simulate the experiments 31

6.3 Running time on the supercomputer . . . 33

1 Squeezed light source

1.1 Squeezed light generation

Fig(S1) illustrates the optical parametric oscillator (OPO) configuration. Squeezed light at 1551.4 nm is generated through type-0 parametric down-conversion by pumping a doubly resonant OPO with 775.7 nm light below threshold. The OPO comprises a hemilithic cavity with a periodically poled potassium titanyl phosphate (PPKTP) crystal as the nonlinear medium, featuring a planar facet with an anti-reflection coating and a curved facet with a high-reflection coating. The output mirror has a partially reflective coating. Crystal dimensions and coating parameters are detailed in Table S2. The cavity exhibits a round-trip optical path length of approximately 40.4 mm, yielding a free spectral range of 7.4 GHz and a finesse of 59 for the fundamental mode and 29 for the pump mode. Double resonance is achieved by precise temperature tuning of the PPKTP crystal.

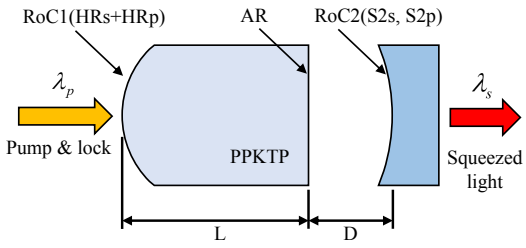

Figure S1: Schematic of the OPO.

Parameter	Value	Parameter	Value
λ_ω	1551.4 nm	ROC2	7 mm
$\lambda_{2\omega}$	775.7 nm	$S2_\omega$	90%
ROC1	12 mm	$S2_{2\omega}$	90%
HR_ω	99.978%	L	10 mm
$HR_{2\omega}$	90%	D	2.1 mm
AR	$< 0.05\%$		

Figure S2: OPO configurations.

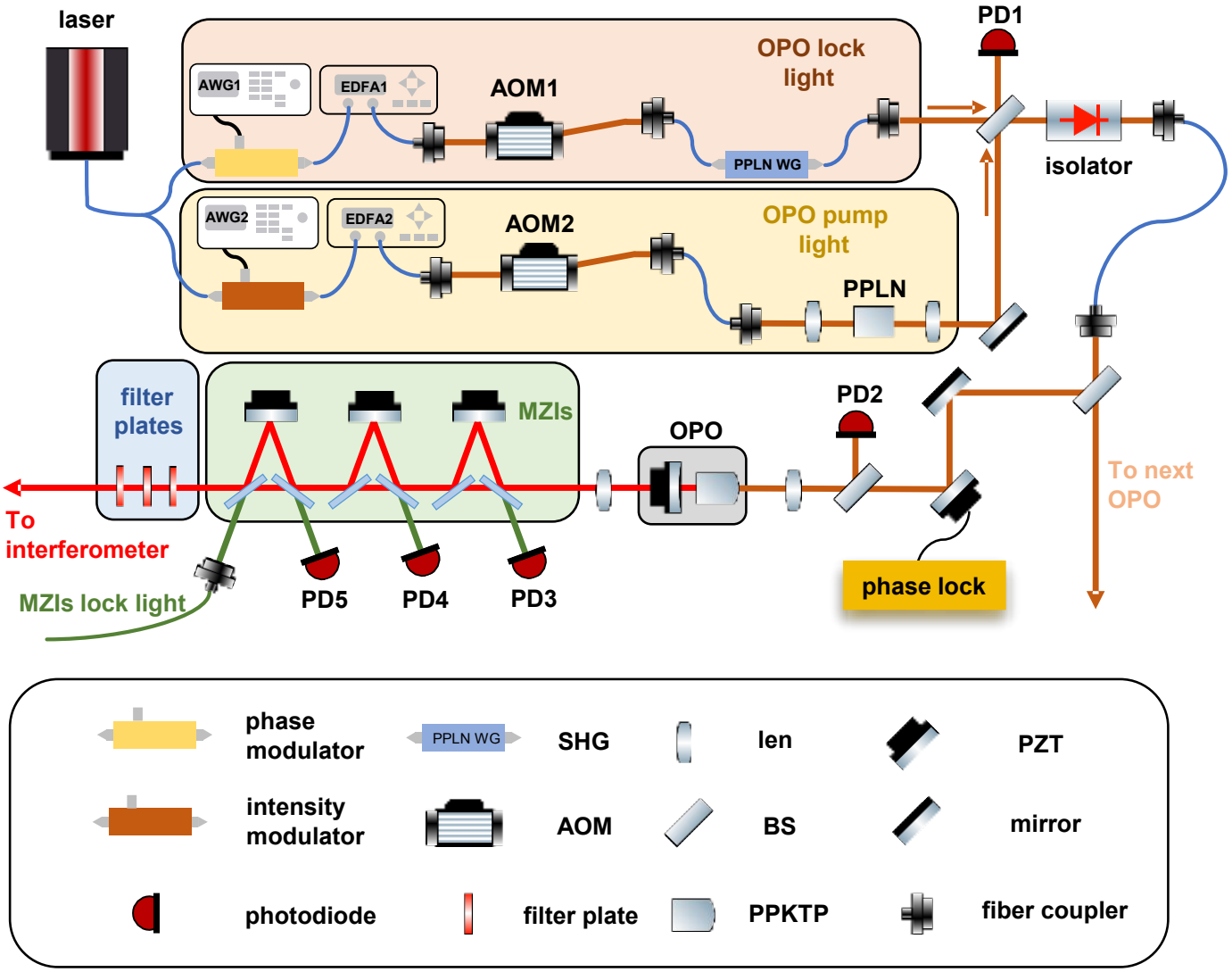

Figure S3: Setup of the squeezed light sources.

Fig.S3 depicts the detailed implementation of squeezed light generation. Rectangular pump pulses of 1.6 ns duration, centered at 775.7 nm, drive the optical parametric oscillators (OPOs) to produce down-converted photons at 1551.4 nm. The pulse duration is configured to satisfy the single temporal mode condition determined by the OPO design. A 50 ns interval between consecutive pulses aligns with the delay loops. A continuous seed laser is modulated into pulses using a 20 GHz lithium niobate electro-optic amplitude modulator (EOM) and amplified by an erbium-doped fiber amplifier (EDFA). The pump light is generated via second harmonic generation (SHG) in a periodically poled lithium niobate (PPLN) bulk crystal. Prior to entering the PPLN crystal, the amplified fundamental beam is controlled by an acousto-optic modulator (AOM), which

serves as a high-speed optical switch to regulate the number of injected pump pulses for varying sampling scales.

The Pound–Drever–Hall (PDH) technique is employed to actively stabilize the optical parametric oscillators (OPOs). The probe light is generated using a process analogous to that of the pump light. A portion of the seed laser is phase-modulated at 100 MHz using an electro-optic modulator (EOM) and amplified by an erbium-doped fiber amplifier (EDFA). The fundamental beam is shaped into 1 µs rectangular pulses and up-converted in a periodically poled lithium niobate (PPLN) waveguide to serve as the PDH lock probe. The two acousto-optic modulators (AOMs) controlling the pump and probe pulses operate at identical driving frequencies and diffraction orders, ensuring the probe and pump share the same center frequency. To prevent crosstalk and stray counts from the probe pulses, the probe and pump pulses are temporally separated, as shown in Fig. **??**. The probe and pump beams are combined using a variable beam splitter, with the cost of discarding a small part of pump laser.

1.2 Filtering of non-degenerate spectral modes

The down-converted photons generated by the optical parametric oscillators (OPOs) encompass numerous spectral modes resonant with the cavity, with only the zeroth-order degenerate mode constituting the single-mode squeezed state. Consequently, a spectral filtering system is essential to suppress unwanted non-degenerate components. To address spectral modes with a free spectral range of less than 10 GHz, cascaded Fiber Bragg Gratings (FBGs) are conventionally employed. However, the transmission efficiency of current FBGs falls short of the high system efficiency required. To achieve narrowband filtering with minimal photon loss, we implement cascaded unbalanced Mach-Zehnder interferometers (MZIs). By introducing an optical delay difference L between the MZI arms, the transmission at one output port exhibits a sinusoidal frequency dependence,

$$T(\nu) = \frac{1}{2} + \frac{1}{2}\cos\left(\frac{2\pi L}{c}(\nu - \nu')\right) \tag{S1}$$

where L is tuned to be the same as the cavity length L_c , and the cavity's zeroth order spectral mode centered at ν_0 attains a unity transmission at the target output port, i.e, $\nu' = \nu_0$, then the frequency centered at $\nu_0 \pm \frac{c}{2L_c}, \nu_0 \pm \frac{3c}{2L_c}, \nu_0 \pm \frac{5c}{2L_c}, \ldots$ acquire a π phase and are annihilated from

this port by destructive interference, which exactly correspond to the $\pm1, \pm3, \pm5, \ldots$ order spectral mode of the cavity. Generally, an MZI with $L = \frac{2n+1}{2^n} L_c$ filters out the spectral modes of order $\pm 2^n, \pm 3 \times 2^n, \pm 5 \times 2^n \ldots$.

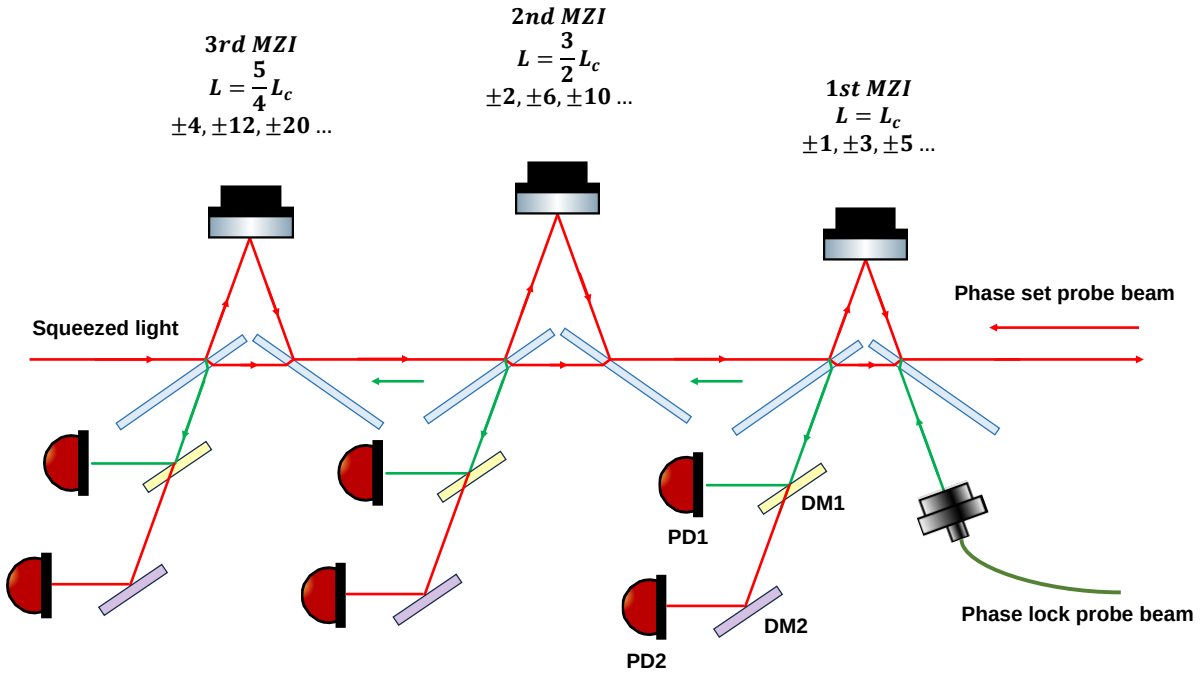

Figure S4: Setup of the unbalanced MZIs for filtering.

The configuration of the unbalanced Mach-Zehnder interferometers (MZIs) for spectral filtering is illustrated in Figure S4. For each optical parametric oscillator (OPO), three cascaded unbalanced MZIs with optical path differences of $L = L_c, \frac{3}{2} L_c, \frac{5}{4} L_c$ are implemented, effectively suppressing most non-degenerate spectral modes, except for orders $\pm 8, \pm 24, \pm 40, \ldots$. Each MZI is comprised of two balanced beam splitters and a mirror, forming a specially-designed triangular interference structure. Incidence angle of the mirror is 20.6°, such a configuration guarantees that the incidence angle on the beam splitter equals to the brewster angle (55.3°). Thus, if the incident beam has a p-polarization, which is exactly the status in the experiment, nearly zero undesired reflection loss on the non-functional optical surface can be realized without anti-reflection coating. Precise phase control, critical for efficient filtering, is achieved by mounting a mirror on the longer MZI arm to a piezoelectric transducer (PZT) for accurate phase tuning and active stabilization. Phase setting and locking utilize two counter-propagating probe beams, detected at the secondary output port of

each MZI. A probe beam at 1064 nm, coupled into the single-mode squeezed state (SMSS) path at the third MZI, is partially extracted for photodiode-based feedback monitoring, with the remainder propagating to subsequent MZIs for recursive probing. For phase tuning, a back-propagating probe beam, matched in path, frequency, and polarization to the squeezed light, is injected. The phase is adjusted by modulating the active lock setpoint to minimize the probe intensity detected by the corresponding photodiode. Dichroic mirrors separate the probe laser from the squeezed light before detection to prevent crosstalk. The phase setting and stabilization precision are estimated to be within $\pm\lambda/1200$ at 1550 nm. Three layers of 0.4 nm narrow band pass filters follow to further eliminate residual undesired spectral components.

With carefully tuned mode matching of each MZI to be above 99.95% and an average transmission of the narrow band pass filters beyond 98.5%, we report a >40 dB rejection ratio of all high-order spectral modes and an overall filtering transmission above 95%.

1.3 Theoretical simulation of the joint spectral property of the squeezed light sources

Compared to the continuous joint spectrum of spontaneous parametric down-conversion (SPDC), the resonance cavity imposes a frequency grid defined by the resonance condition. By selecting an appropriate pump linewidth, only diagonal frequency modes, such as (0,0), (+1,–1), (+2,–2), and higher orders, are retained. These modes exhibit nearly identical squeezing parameters due to the gradual variation of the phase-matching function. Cascaded narrow-band filters and unbalanced Mach-Zehnder interferometers subsequently suppress all modes except the (0,0) mode, yielding a single-mode squeezed state as the experimental squeezed light source.

The (0,0) mode retains a fine internal spectral structure, primarily responsible for reduced spectral purity. In the low-gain regime, the joint spectrum results from the product of the transmission spectra of the two parametric beams and the pump spectrum. The -45° orientation of the pump spectrum prevents direct factorization into two independent functions, leading to a Schmidt decomposition that produces multiple frequency modes with varying amplitudes. As pump power increases, the squeezing parameters r of these modes scale proportionally. Given the exponential relationship between photon number, $n = \sinh^2(r)$ and the squeezing parameter r, spectral purity

approaches unity with higher pump power.

However, the predicted increase in spectral purity does not fully align with experimental results, as the model overlooks time-ordering effects [1], which are significant in optical parametric oscillator (OPO) systems and must be included in theoretical simulations. Time ordering introduces cubic and higher odd-order terms in the relationship between the squeezing parameter and pump field intensity. This behavior can be numerically modeled using the Heisenberg equations [2].

The Heisenberg equation for the single-mode SPDC (the dispersion term is neglected because it's insignificant within a single FWHM) and the boundary conditions are:

$$\frac{\partial}{\partial z}a_k(z,\omega) = \mathrm{i}\gamma \int \mathrm{d}\omega' \beta_k(\omega+\omega') a_k^\dagger(z,\omega') \tag{S2}$$

$$a_1(0,\omega) = a_{-1}(0,\omega) \tag{S3}$$

$$a_{-1}(L,\omega)\mathrm{e}^{-\mathrm{i}\omega L} = r a_1(L,\omega)\mathrm{e}^{\mathrm{i}\omega L} + t a_i(\omega) \tag{S4}$$

$$a_o(\omega) = -t a_1(L,\omega)\mathrm{e}^{\mathrm{i}\omega L} + r a_i(\omega) \tag{S5}$$

Here, a denotes the annihilation operator for the down-converted photons, β represents the pump light spectrum, L is the cavity length, γ is the nonlinear coefficient, r and t are the reflectance and transmittance of the cavity mirrors, respectively, and z is the spatial coordinate along the light propagation direction within the PPKTP crystal. The parameter $k = \pm 1$ distinguishes the two counter-propagating beams within the cavity. The divergence of the Gaussian beam inside the PPKTP crystal is neglected, as its spectral impact occurs on a scale significantly larger than the free spectral range (FSR).

Furthermore, the above equations can be discretized and then solved numerically:

$$\mathbf{u}_{n,k}(z) = a_k(z,\omega_n)$$
$$\mathbf{v}_{n,k}^\dagger(z) = a_k^\dagger(z,\omega_n)$$

$$\begin{pmatrix}\mathbf{u}_k(z)\\ \mathbf{v}_k^\dagger(z)\end{pmatrix} = \mathrm{e}^{\mathrm{i}Q_k l}\begin{pmatrix}\mathbf{u}_k(z)\\ \mathbf{v}_k^\dagger(z)\end{pmatrix}$$

$$\begin{pmatrix}\mathbf{u}_{-1}(z)\\ \mathbf{v}_{-1}^\dagger(z)\end{pmatrix} = rU_\phi\begin{pmatrix}\mathbf{u}_1(z)\\ \mathbf{v}_1^\dagger(z)\end{pmatrix} + t\begin{pmatrix}\mathbf{u}_i\\ \mathbf{v}_i^\dagger\end{pmatrix}$$

$$\begin{pmatrix} \mathbf{u}_o \\ \mathbf{v}_o^\dagger \end{pmatrix} = -tU_\phi \begin{pmatrix} \mathbf{u}_1(z) \\ \mathbf{v}_1^\dagger(z) \end{pmatrix} + r \begin{pmatrix} \mathbf{u}_i \\ \mathbf{v}_i^\dagger \end{pmatrix} \tag{S6}$$

Here, Q comes from the discretization of Eq.S2, U_ϕ comes from the discretization of the boundary conditions Eq.S4 and l represents the length of PPKTP. Solving the above matrix equation yields the unitary operator for the entire process:

$$\begin{pmatrix} \mathbf{u}_o(z) \\ \mathbf{v}_o^\dagger(z) \end{pmatrix} = \frac{r - U_\phi e^{iQ_1 l} e^{iQ_{-1} l}}{I - rU_\phi e^{iQ_1 l} e^{iQ_{-1} l}} \begin{pmatrix} \mathbf{u}_i(z) \\ \mathbf{v}_i^\dagger(z) \end{pmatrix} \tag{S7}$$

Finally, performing the Schmidt decomposition on $\mathbf{u}_o$ will yield the spectrum and squeezing parameter of each Schmidt mode, which further leads to the relationship between the spectral purity and the pump power.

1.4 Measurement of the spectral purity

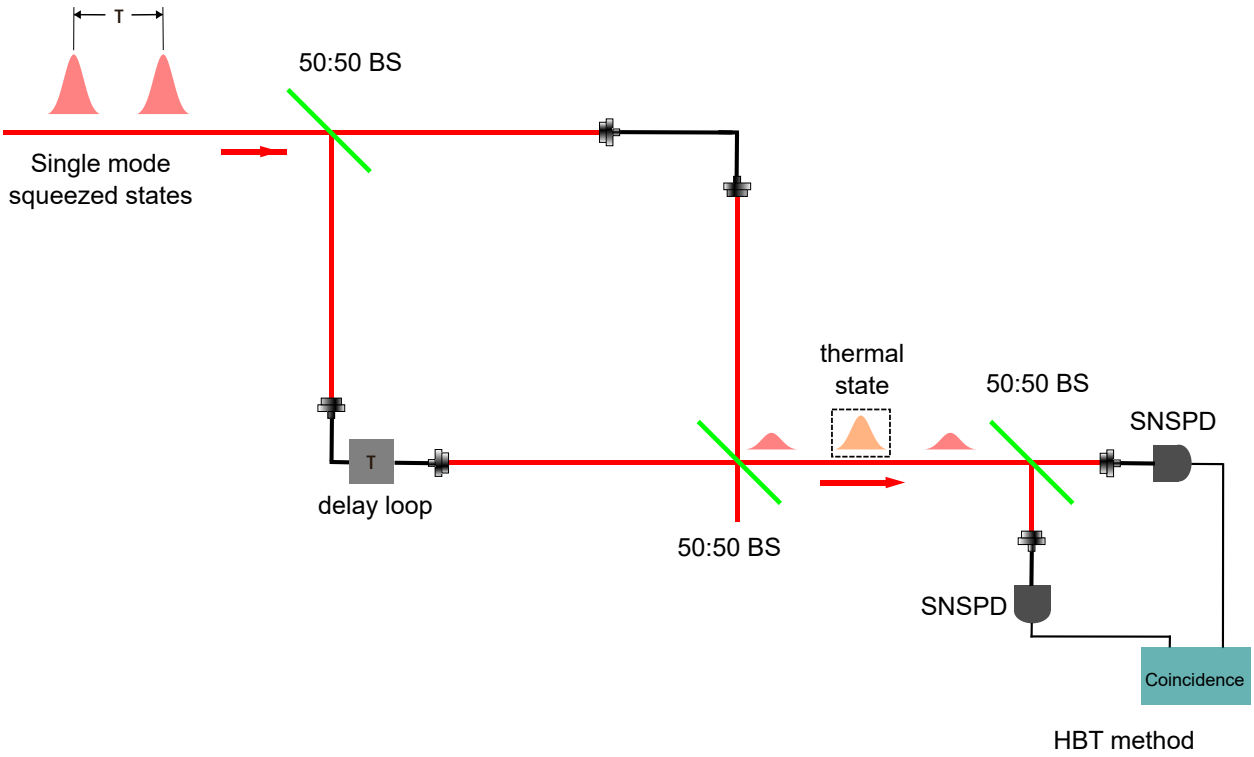

Figure S5: Measurement of the squeezed light sources' spectral purity.

Spectral purity of the squeezed light sources is quantitatively calibrated using unheralded second-order correlation measurements, implemented via a Hanbury-Brown-Twiss (HBT) experiment on thermal states generated by interfering two single-mode squeezed states. The measurement setup, illustrated in Figure S5, consists of two cascaded 50:50 balanced two-mode interferometers interconnected by fiber delay loops with a time delay difference of τ. When two single-mode squeezed state pulses, separated by τ, traverse the circuit, the second pulse interferes with the first at the second interferometer, each with 50% transmission. With the interference phase correctly set, two independent thermal states are produced at the output ports. As thermal states remain invariant under arbitrary transmission losses, such losses do not affect the calibration. The thermal state from one output port is selected and analyzed using a 50:50 beam splitter in an HBT configuration to measure the second-order correlation.

We model the thermal state as a mixing of a major mode with mean photon number $\bar{n}$ and a distinguishable minor mode with mean photon number $\bar{m}$, where $\bar{m} << \bar{n}$. $\bar{n}$ and $\bar{m}$ can be numerically solved from the measured second-order correlation function $g_2(0)$ and the click probability p at one port:

$$g_2(0) = \frac{(2+\bar{n})(2+\bar{m})(2(\bar{n}^2+\bar{m}^2)+2\bar{n}\bar{m}+3(\bar{n}^2\bar{m}+\bar{m}^2\bar{n})+\bar{n}^2\bar{m}^2)}{(1+\bar{n})(1+\bar{m})(\bar{n}\bar{m}+2(\bar{n}+\bar{m})^2} \tag{S8}$$

$$p = \frac{2(\bar{n}+\bar{m})+\bar{n}\bar{m}}{(2+\bar{n})(2+\bar{m})} \tag{S9}$$

We mainly care about the ratio of the distinguishable minor component,

$$R_{\bar{n}} = \frac{\bar{n}}{\bar{n}+\bar{m}} \tag{S10}$$

and the spectral purity, which is defined as:

$$\mathbb{P} = \frac{\bar{n}^2+\bar{m}^2}{(\bar{n}+\bar{m})^2} \tag{S11}$$

1.5 Measured spectral purity under different squeezing level

The measurement is conducted for both interference of a single OPO, which follows the delayed scheme in Sec.1.4, and direct interference between two independent OPOs. The two cases give the nearly identical results and coincide well with the theoretical simulation(S6).

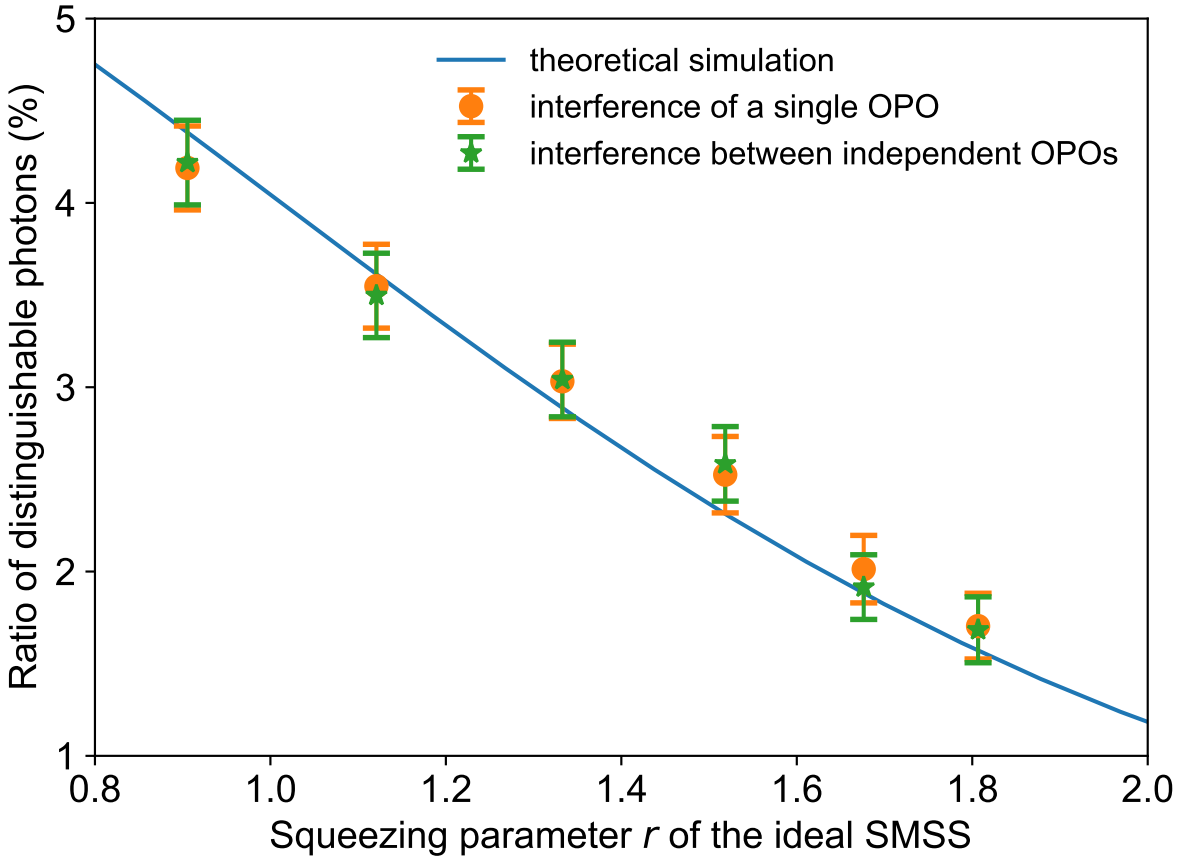

Figure S6: Measured spectral purity under different squeezing level. The error bars are obtained from repeated data collection and processing.

1.6 Measured spectral purity under different temporal delay

The circuit architecture relies on long-range temporal interference, raising concerns about whether extended temporal delays compromise interference indistinguishability. To investigate, we measured spectral purity using temporal interference with delay lengths of 50 ns, 800 ns, and 12 800 ns, the latter being the maximum delay in our circuit. Results presented in Fig. S7, show nearly identical spectral purity across all delay lengths, indicating that temporal delays within our circuit's range do not observably degrade the indistinguishability of squeezed light pulses generated at different times.

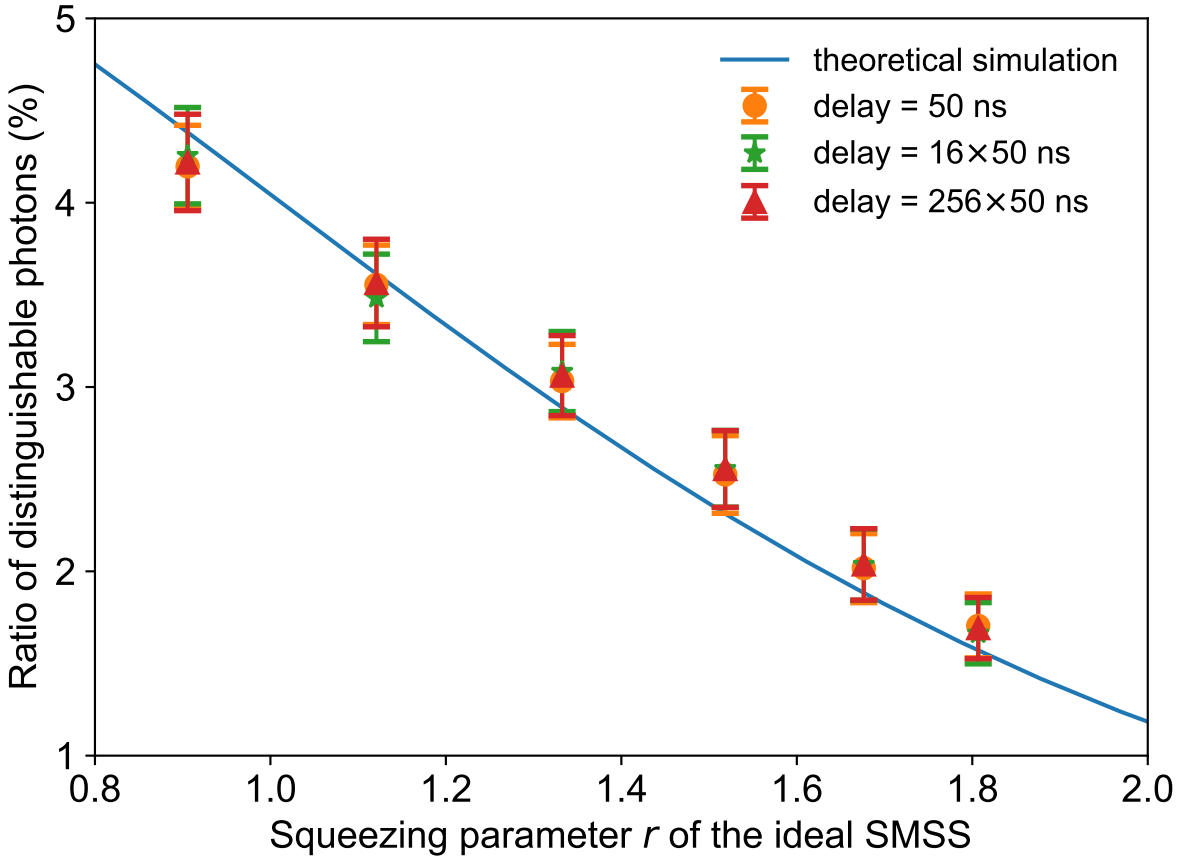

Figure S7: Measured spectral purity under different temporal delay.

2 Ultra-large programmable photonic circuit

2.1 Spatial-temporal hybrid interference network

The circuit architecture, depicted in Figure S8, comprises three cascaded ultra-low-loss, fully connected 16-mode interferometers interconnected by two delay loop arrays. Each interferometer is fabricated with a multi-layer Mach-Zehnder-type interference structure, which features both compactness and compatibility with external thermal tunability. The transmission efficiency of each 16-mode interferometer is 99% per mode, with an average wave-packet overlap exceeding 99.7%. The delay loop arrays form arithmetic progressions with common differences of τ for the shorter array and 16τ for the longer array, where $\tau = 50\,\text{ns}$ is set to match the recovery time of single-photon detectors. Photons traversing the first interferometer and short delay loop array are split into 16 sub-beams, arriving at time bins $[t, t+\tau, \ldots, t+15\tau]$. These sub-beams then enter the second interferometer and long delay loop array, where the i-th loop directs beams to time bins $[t+i\times 16\tau, t+(1+i\times 16)\tau, ..., t+(15+i\times 16)\tau]$. This configuration enables each input mode to couple densely to the subsequent 16^2 temporal modes and redistribute across all 16 spatial modes via the third interferometer

2.2 Programmability of the system

The system's programmability, illustrated in Figure S9, enables flexible configuration of input sequences for single-mode squeezed states (SMSSs). By controlling the fiber electro-optic modulator (EOM) that shapes the seed laser and the free-space acousto-optic modulator (AOM) that switches the fundamental beam output from the erbium-doped fiber amplifier (EDFA), the SMSS input sequence can be tailored for sampling tasks with varying input scales and optimized repetition rates.

The three 16-mode interferometers, equipped with thermally tunable components, enable reconfiguration through thermal control. The interference network's phase parameters are programmable in two ways. First, the center frequency of each single-mode squeezed state (SMSS) pulse can be adjusted by modulating the acousto-optic modulator (AOM) driving signal, effectively altering the phase between temporal modes due to delayed interference. Second, the phases of the four optical

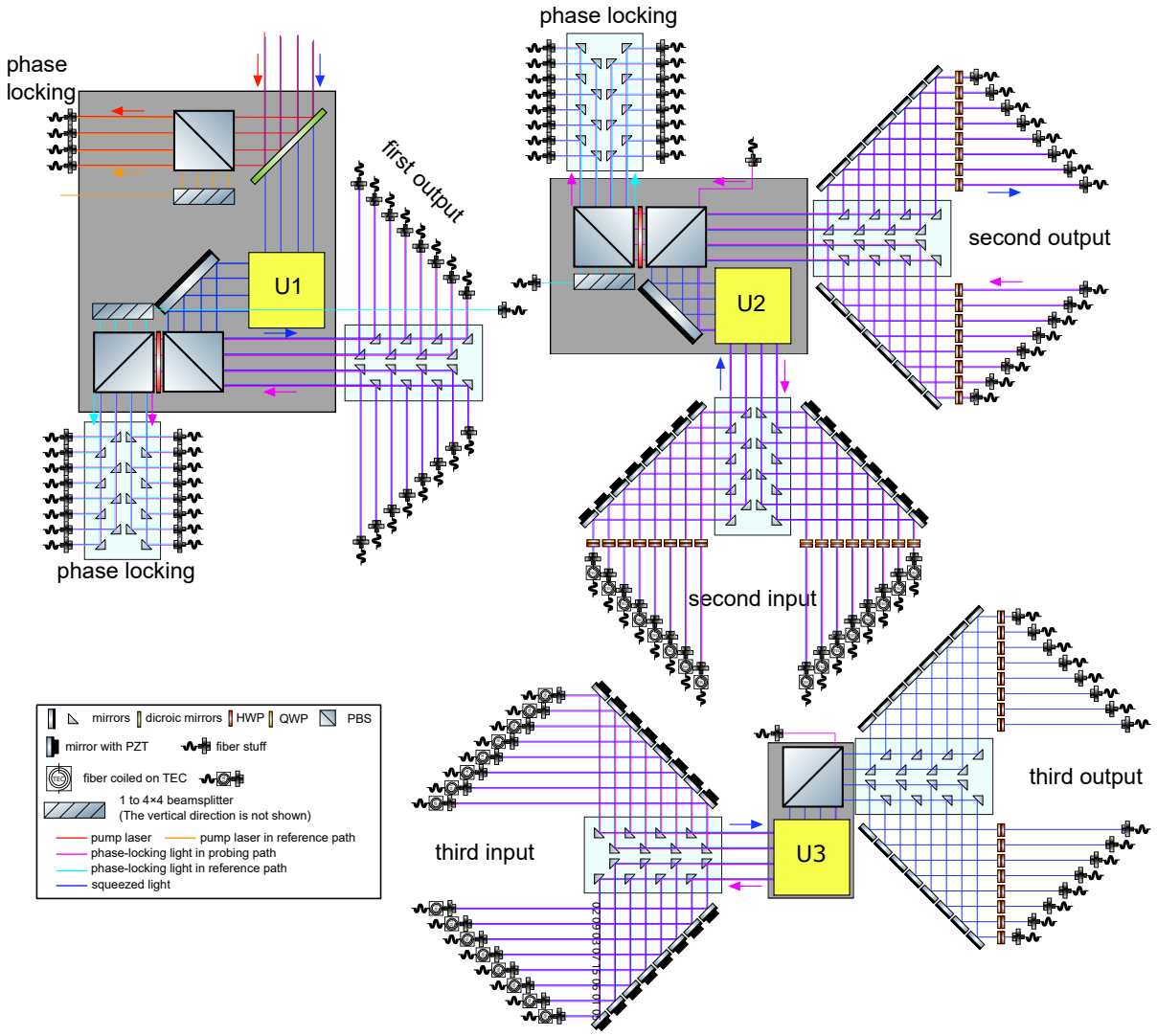

Figure S8: Detailed setup of the photonic circuit, which comprises three cascaded interferometers. Squeezed states traverse these components, interconnected by delay loops. Concurrently, pulsed light of identical wavelength counter-propagates with the squeezed light to stabilize the phase of the delay loops. Mirror positions are adjusted in the schematic for clarity. The thickness of light rays indicates whether the light is single-layered or multi-layered in the vertical direction.

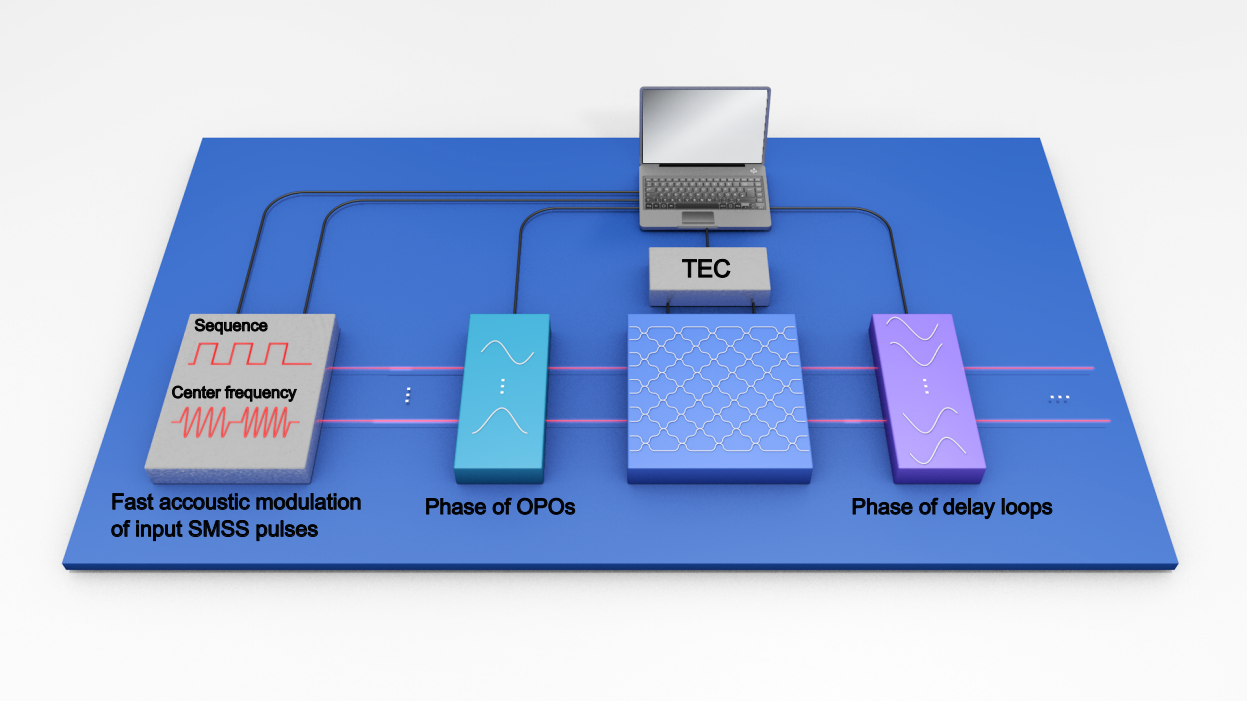

Figure S9: Programmability of the system.

parametric oscillators (OPOs) and two delay loop arrays can be arbitrarily set by configuring the corresponding phase-lock module setpoints. These phase control mechanisms provide vast degree of programmability freedom of the circuit's phase parameters.

Before the experiments, we reset all the programmable parameters of the circuit and fix the parameter status during data acquisition and calibration of the transformation matrix.

2.3 Phase stabilization of the circuit

Phase stabilization is critical for GBS experiments. Our system incorporates three active servo loop modules for phase locking, ensuring the stability of the entire interference network.

The first phase-lock module stabilizes the phase from the initial splitting of pump pulses to the first interferometer, as depicted in Figure S10. A mirror mounted on a piezoelectric transducer (PZT) is positioned in the pump beam's path to each optical parametric oscillator (OPO). As the pump beam co-propagates with the squeezed light through the cavities, it serves as an ideal probe for feedback. A dichroic mirror, transparent at 1550 nm but reflective at 775 nm, separates the pump light, which is then interfered with a reference beam. The error signal, obtained via balanced

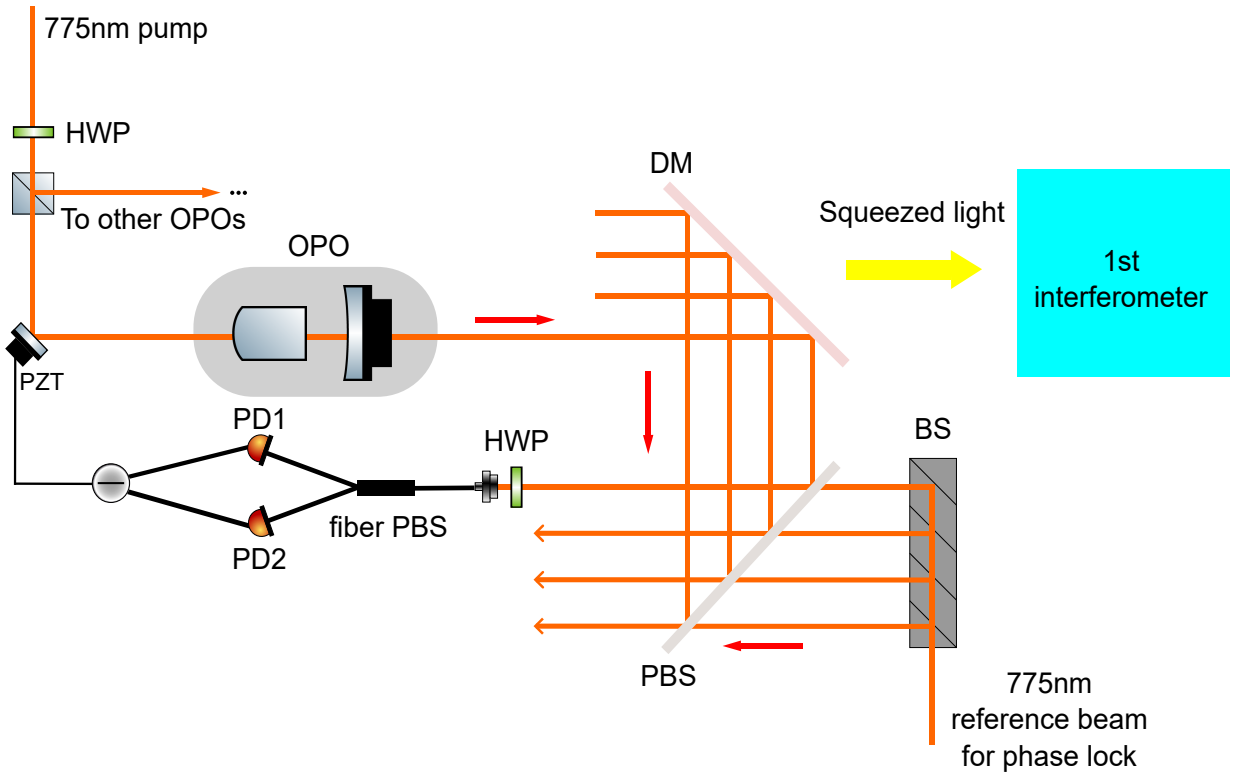

Figure S10: Setup of phase lock before the first interferometer.

homodyne detection, is compensated by adjusting the PZT displacement.

The second and third phase-lock modules stabilize the phases of the two fiber delay loop arrays, as illustrated in Figure S11. Using the first array as an example (with the same method applied to the second), a piezoelectric transducer (PZT)-mounted mirror is positioned in each spatial mode's path for active phase compensation. A counter-propagating probe beam, matched in frequency but orthogonally polarized to the squeezed light, is split into 16 beams and coupled to each spatial mode at the second interferometer's input via a polarization beam splitter. The probe beam, pulsed using an acousto-optic modulator (AOM) and temporally offset from the squeezed light pulse train to minimize stray counts, is separated at the first interferometer's output by another polarization beam splitter and interfered with a reference beam to generate an error signal. This signal drives PZT adjustments. To address significant phase drift in long fibers due to temperature fluctuations, which exceeds single-PZT compensation, a thermoelectric cooler (TEC) feedback system mitigates

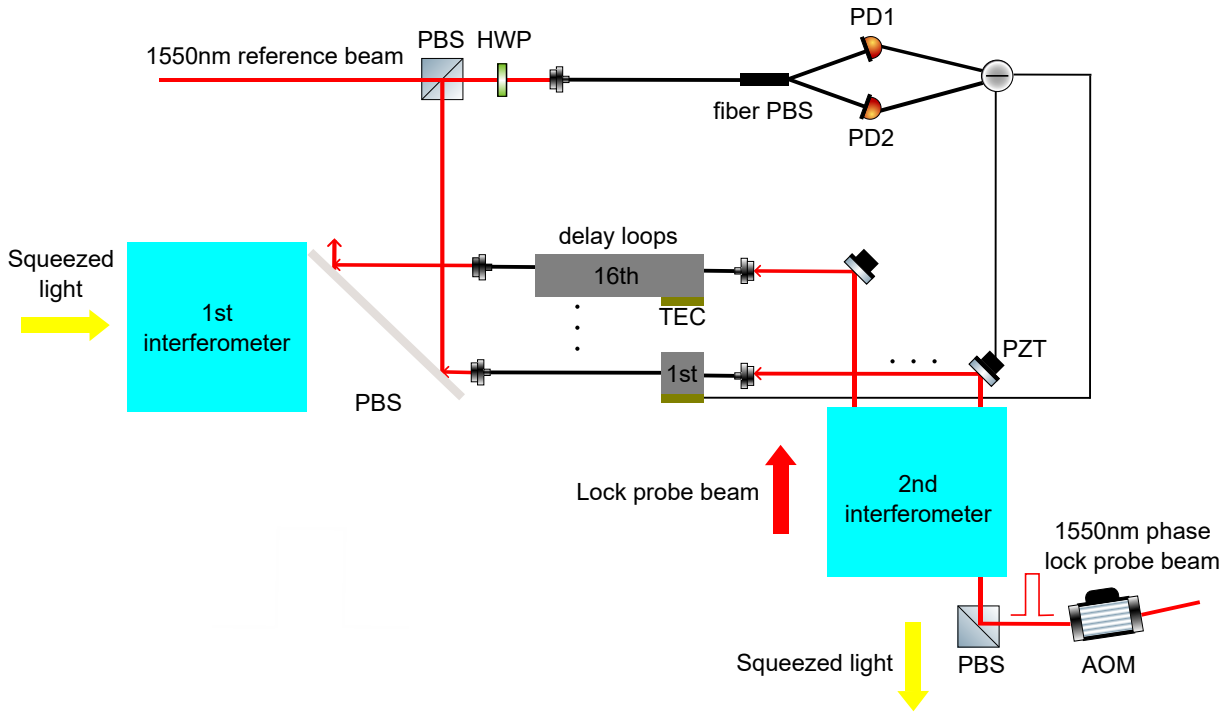

Figure S11: Setup of phase lock between the interferometers.

slow thermal drift. Phase-lock precision is estimated at 3 nm for the first delay loop array and 10 nm for the second.

2.4 Fast feedback of seed laser frequency by referencing to an ultra low expansion (ULE) cavity

The large time delay of the circuit imposes high requirement of the stability on the laser frequency, since the drift of frequency will be amplified by the long-delayed temporal interference and eventually converted to phase noise. The longest time delay in the circuit is 256×50 ns, which means frequency fluctuation of approximately 100 kHz would induce a 2π phase change at 1550 nm. Considering the frequency noise of commercial DFB laser which drifts over several kilohertz in short time scale of tens of microseconds, the resultant phase noise in long-range temporal interference is notable and too fast to be compensated with piezo actuators. To suppress this noise, we reference the

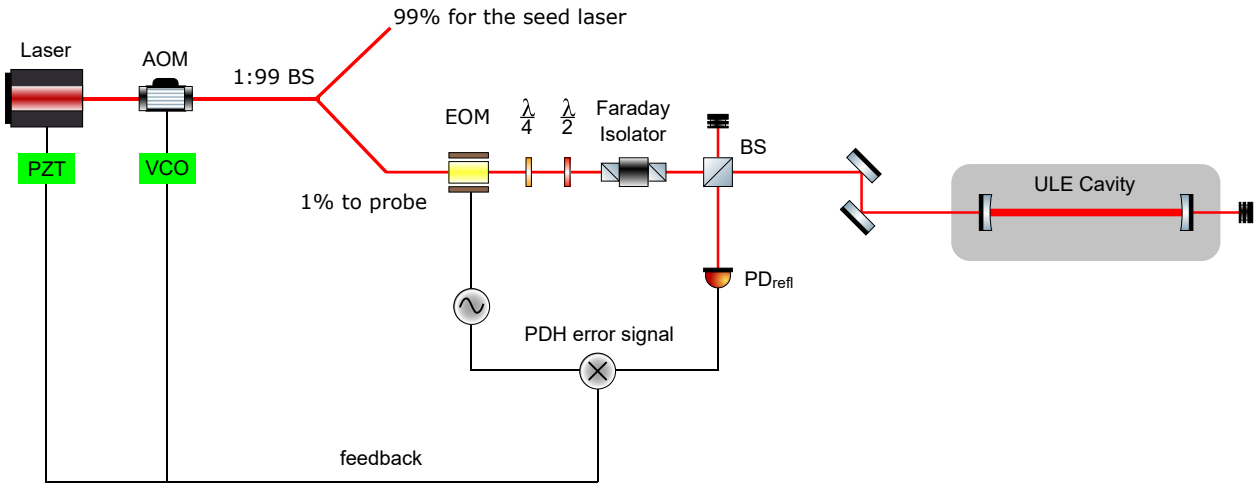

Figure S12: Stabilization of the laser frequency.

center frequency of the seed laser to an ultra low expansion (ULE) cavity to get the error signal by Pound–Drever–Hall (PDH) technique, and compensate the frequency fluctuation with a cascaded feedback system. An fiber AOM driven by a voltage controlled oscillator (VCO) is used for the fast frequency modulation, and a piezo actuator co-packaged in the DFB laser module is responsible for the slower but GHz-range frequency compensation. The detailed setup is depicted in S12.

3 Calibration of the transformation matrix

The circuit's spatial-temporal hybrid encoding enables factorization of both input and output modes into spatial and temporal dimensions. The input comprises $M_s \times M_t$ modes, where M_s denotes the number of utilized spatial input ports of the first interferometer (or optical parametric oscillators) and M_t represents the number of temporal inputs, determined by the number of pump pulses. Given the circuit's maximum time delay, an input of M_t pump pulses generates a sequence of squeezed light pulses spanning M_t temporal modes, resulting in photons distributed across $M_t + 255$ output temporal modes. With the final interferometer's 16 spatial modes, the total output modes are $16 \times (M_t + 255)$. The interference network's transformation matrix, with input modes as rows and output modes as columns, has dimensions $M_s \times M_t$ rows and $16 \times (M_t + 255)$ columns.

The circuit's architecture enables coupling of each input mode to $256 \times 16 = 4096$ output modes. Given the fixed circuit and high symmetry of temporal encoding, the interference matrix for a single input temporal mode—a kernel matrix of dimensions $M_s \times 4096$ —is sufficient to characterize the system. The full interference matrix is constructed by iteratively repeating and displacing this kernel for all input temporal modes.

3.1 Measurement of the matrix amplitude

To measure the matrix amplitude (beam coupling ratio), a sequence of squeezed light pulses from a single optical parametric oscillator (OPO) is input with a temporal interval exceeding the maximum connectivity of the fiber delay loops, ensuring no internal interference occurs. Given the circuit's large scale, a single pulse input yields low count rates per output mode. Sufficient data are collected to minimize statistical fluctuations, with stray counts subtracted. The matrix amplitude is determined by first calibrating the input pulses' squeezing parameter, optimized by fitting the measured click rate and photon number distribution.

A:For a given squeezing r_{try}, calculate the coupling ratio M_{try} by the measured click probability for all output modes;

B:Numerically compute the theoretical photon number distribution PND_{try} from r_{try} and M_{try};

C:Calculate the total variation distance(TVD) between PND_{try} and the photon number dis-

tribution PND_{exp} counted from the experimental data.

By the method, there will be an optimal squeezing parameter which attains a minimum TVD value. Repeat step A to step C by linear search until the optimal input squeezing is found with sufficient precision.

Once the squeezing parameter of the input pulses is determined, the coupling ratios for all 4096 output modes are derived directly from the measured click probabilities. This procedure is repeated for each optical parametric oscillator (OPO) input to obtain the 4×4096 kernel matrix of amplitudes. The overall system transmission for each OPO is calculated by summing the 4096 elements in the corresponding row of the kernel matrix.

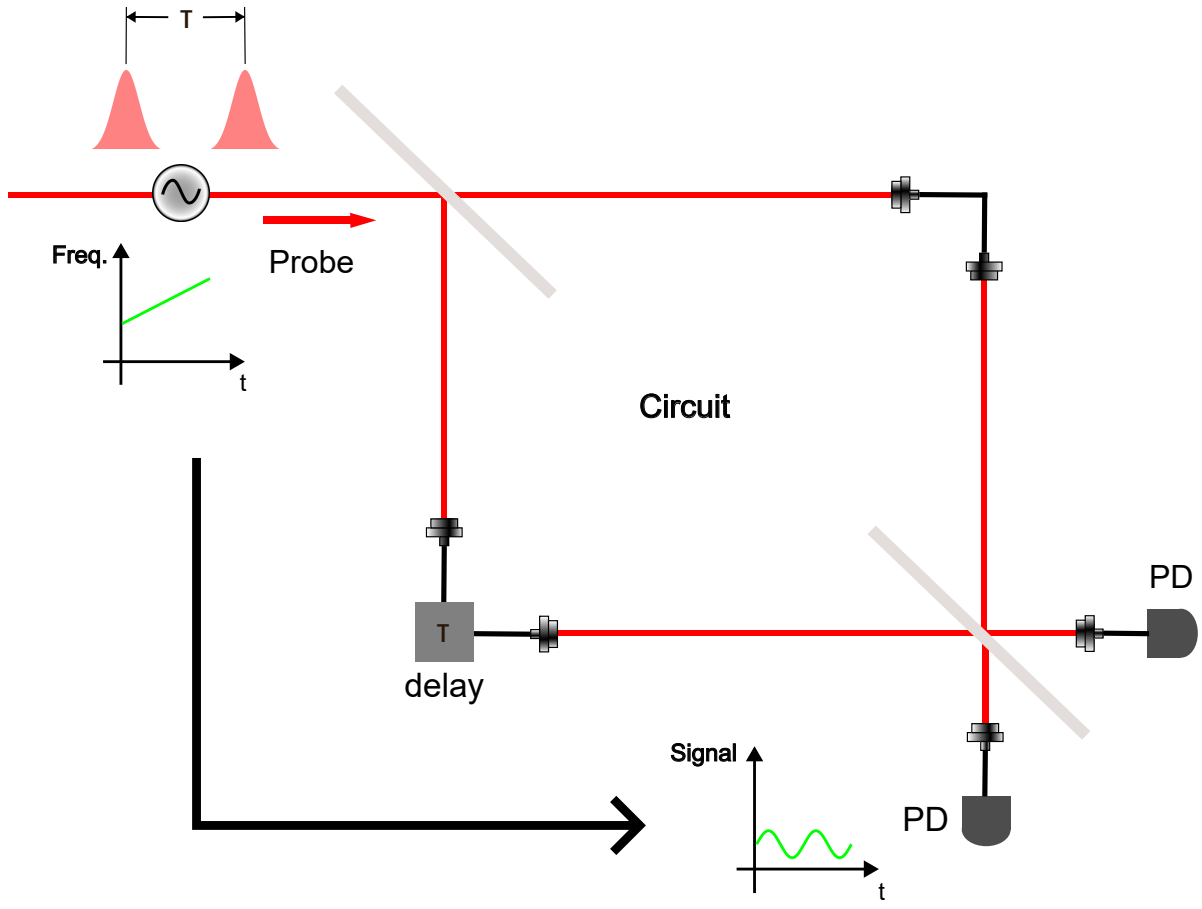

Figure S13: Frequency-swept laser pulses for phase measurement.

3.2 Measurement of the matrix phase

The interference network's phase elements are determined by analyzing two components: the internal circuit phase and the phase from squeezed light generation to circuit entry. Still we focus on how to obtain the 4×4096 kernel of the entire phase matrix.

3.2.1 Measurement of phase inside the circuit

Frequency-swept laser pulses, matched to the circuit's temporal encoding, are injected to interfere within the network and probe phase information. The temporal delay makes frequency sweeping equivalent to actively scanning the interference phase, yielding periodic interference patterns (Fig. S13). By precisely referencing the probe laser's frequency to that of the squeezed light, the phase

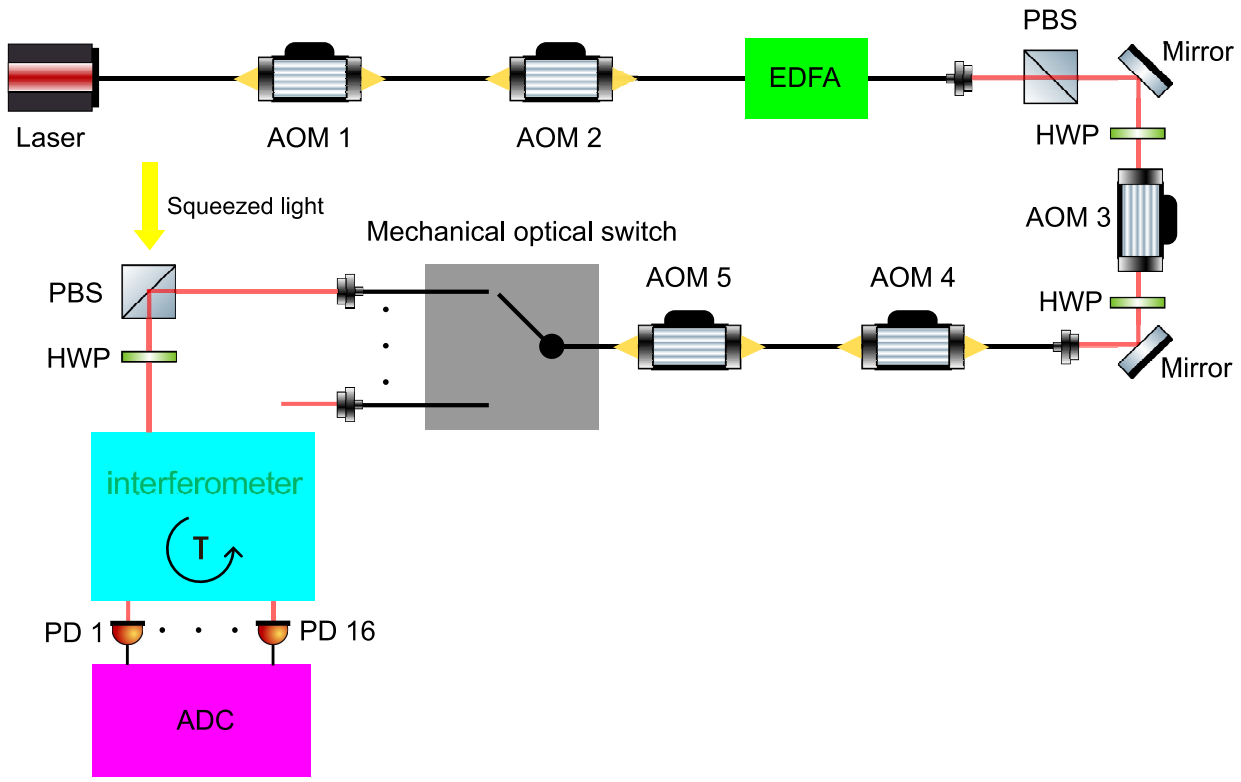

Figure S14: Setup of measurement of the phase inside the circuit.

experienced by the squeezed light within the circuit is directly extracted from the measured curves.

The phase measurement setup, illustrated in Fig. S14, employs two fiber acousto-optic modulators (AOMs) operating at $400M \pm 100$ MHz, providing a frequency sweep range of up to 200 MHz. The frequency-modulated output is amplified by an erbium-doped fiber amplifier (EDFA) and shaped into 25 ns rectangular pulses using three additional AOMs. AOM4 and AOM5, fiber-based AOMs driven at 400 MHz with a 6 ns rise/fall time and >50 dB extinction ratio, generate high-quality pulse sequences. AOM3, a free-space AOM synchronized with AOM4 and AOM5, acts as a light switch to protect the fiber AOMs from continuous high-power laser input. The diffraction frequencies of all AOMs are calibrated to align the sweep's zero point with the squeezed light's center frequency.

The probe beam is coupled to the squeezed light's path via a polarization beam splitter before the first interferometer, followed by a half-wave plate (HWP) to rotate the polarization. During

measurement, laser pulses are injected into a single input port, with a micro-mechanical light switch automating iteration across all input ports. Light signals are detected by two 8-channel photodetectors with a 200 MHz bandwidth, and their outputs are processed by two 8-channel analog-to-digital converter (ADC) boards with a 250 MHz sampling rate for data acquisition.

For each spatial input port, the circuit interconnects 256 temporal input modes. Relative to the first pulse, interference is measured between the first pulse and each of the subsequent 255 pulses individually. For each of the 255 temporal inputs, double-pulse units with matching delay intervals are repeatedly injected to generate corresponding interference patterns and extract phase information. Frequency sweeping, implemented in linear step mode and precisely referenced to the squeezed light's center frequency, scans hundreds of frequency points for each curve to produce totally millions of sinusoidal curves, each containing at least eight periods. Curve fitting enables retrieval of all interference phases.

The phase matrix is constructed using a decomposition-and-assemble approach. The interference network comprises three cascaded interferometers, M1, M2 and M3, with the phase of the first delay loop array incorporated into M2 and the second into M3 for simplicity. By determining the phase of these interferometers, the phase matrix is assembled directly from the three components. The focus remains on the 4×4096 kernel matrix K.

Without loss of generality, we index the i_{th} spatial input to be the i_{th} input port of the first interferometer M1, which corresponds to $K[i]$, the i_{th} row of the kernel. For the sake of expressional convenience, we further reshape the 4096 elements of $K[i]$ to be a matrix of size (256,16), where the row dimension represents the 256 temporal modes and the column dimension represents the 16 spatial modes of the last interferometer M3. Determined by its path inside the circuit,

$$K[i](j,k) = M1(i, j\%16) + M2(j\%16, j//16) + M3(j//16, k) \tag{S12}$$

where M1,M2,M3 are three 16×16 matrix representing the three interferometers, the first dimension for the input and the second dimension for the output; indexes i,j,k start from 0; % means the mod operation and // means the integer division operation in computer science.

The measurement results are described by a four-dimensional vector $\Phi(i,l,j,k)$, where i denotes the i_{th} input port of M1, l the temporal input dimension, j the temporal output dimension, and k the spatial output of M3. Referenced to the first temporal input, the elements of Φ are

expressed as the sum of contributions from M1,M2 and M3, determined by tracing the pulse paths through the circuit to the corresponding output time and port,

$$\begin{aligned}\Phi(i,l,j,k) =&(M1(i,j\%16) + M2(j\%16, j//16) + M3(j//16,k)) \\ &-(M1(i,(j-l)\%16) + M2((j-l)\%16,(j-l)//16) + M3((j-l)//16,k))\end{aligned} \tag{S13}$$

Phase of the three 16 mode interferometers can be solved from the measurement results. For instance, one choice to yield M1,M2 and M3 is

$$(M1(i,j) - M1(i,0)) - (M1(0,j) - M1(0,0)) = \Phi(i,j,j,0) - \Phi(0,j,j,0) \tag{S14}$$

$$M2(i,j) - M2(0,j) = \Phi(0,i,16\times j + i,0) - (M1(0,i) - M1(0,0)) \tag{S15}$$

$$M3(i,j) - M3(0,j) = \Phi(0,16\times i,16\times i,j) - (M2(0,i) - M2(0,0)) \tag{S16}$$

Actually, the entire elements of Φ is over-complete to solve for M1,M2 and M3 because there are combinatorial number of topologically equivalent relations which can yield the same results as those given in (S14,15,16). We take average over all these equivalent expressions to figure out M1,M2 and M3 which can suppress the statistical fluctuation and refine the calibration precision. Once the elements of M1,M2 and M3 are determined, the matrix kernel of the circuit's phase can be directly calculated by (S13).

3.2.2 Determine the phase of the squeezed light sources

Multiple optical parametric oscillators (OPOs) serve as squeezed light sources in our experiment, each with an individual phase prior to entering the circuit, determined by the pump pulses and the subsequent propagation of squeezed light to the first interferometer. For the i_{th} OPO, this source phase corresponds to an overall phase added to the i_{th} row of the phase matrix's kernel. One OPO is designated as the reference source, and the phases of the others are measured sequentially. This is achieved by performing sampling tasks with only the reference and one other OPO active, with all irrelevant OPOs blocked. The second-order correlation function is computed from experimental data, and the source phase is determined by linearly searching for the value that minimizes the total variation distance between the experimental statistics and theoretical predictions.

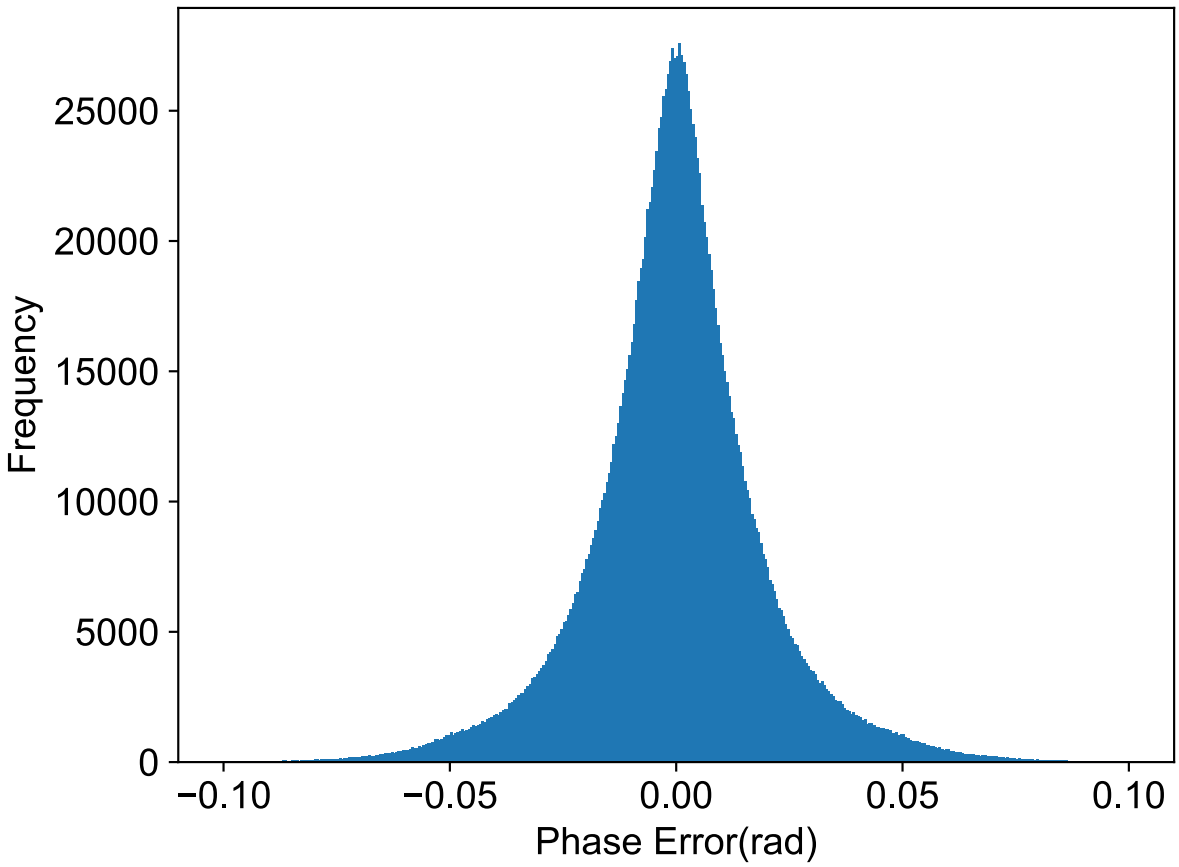

Figure S15: Analyzed phase error of both stablization and calibration of the circuit.

3.2.3 Accuracy of phase stablization and calibration

We analyzed the totally millions of direct phase measurement results, in terms of the intrinsic routing correspondence of the circuit, which yields an overall phase error of both stablization and calibration to be within $\lambda/200$ at 1550nm (S15).

4 Multiple groups of experiments with different circuit depth and input scale

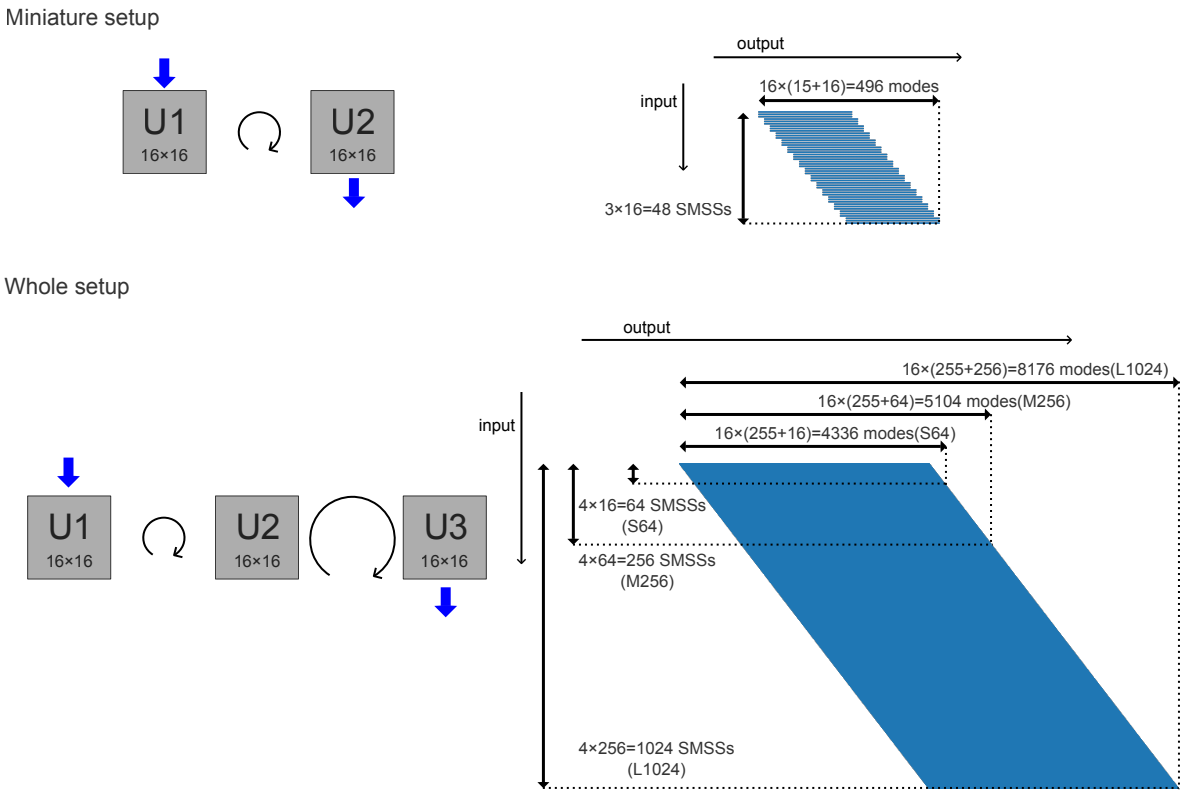

Figure S16: Size of all the groups of experiments with different circuit depth and input scale, illustrated as the point array representation of input and output modes according to the temporal distribution.

We collected multiple groups of data under different circuit depth and input scales to fully characterize and validate the performance of our quantum processor, as illustrated in Fig.S16. We first finished a group of experiments under the miniature setup with a shallower circuit consisting of the first two interferometers, which contains $3 \times 16 = 48$ input SMSSs and $16 \times (16 + 15) = 496$ output qumodes. For the whole setup comprised of all the three interferometers, experiments under three groups of progressively expanding input scale were conducted : the S64 group with $4 \times 16 = 64$ input SMSSs and $16 \times (16 + 255) = 4336$ output qumodes; the M256 group with $4 \times 64 = 256$ input SMSSs and $16 \times (64 + 255) = 5104$ output qumodes; the L1024 group with $4 \times 256 = 1024$ input SMSSs and $16 \times (256 + 255) = 8176$ output qumodes. Photon number distribution of all the

three groups of experiments are shown in Fig.S17.

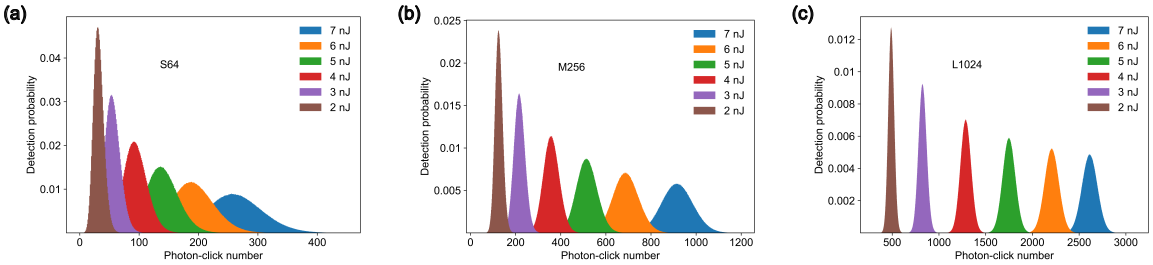

Figure S17: Experimental photon-click number distribution under different pump intensity for all the three input scale of the whole setup. The level of pump intensity is represented by the energy of a pump laser pulse to generate a single SMSS pulse.

5 Partial photon indistinguishability model

We model partial photon indistinguishability in the experiment, attributing noise to the non-ideal joint spectrum of spontaneous parametric down-conversion (SPDC), characterized by its spectral purity. Each source's independent spectral modes, varying in squeezing parameters, traverse the same photonic circuit and detection system. To account for detection, we model virtual arrays of SNSPDs at the circuit's output, each corresponding to a spectral mode. The final output results from a logical OR operation on signals from all detector arrays.

Mathematically, since these spectral modes are independent, the quantum state is the direct product of the state of different spectral modes. We denote the set of the spectral modes by the index $m \in \{1, 2, \cdots, M\}$, where M is the quantity of the spectral modes. The density operator of the system is $\rho = \otimes_{m=1}^{M} \rho_m$. And the output state going through the linear interferometer in the form of covariance matrix is $V_{out} = \oplus_{m=1}^{M} V_m$. Each V_m can be independently calculated by the evolution of the light sources in the circuit.

The original GBS outcome probability of threshold detection is given by *Torontonian*

$$p(S) = \frac{\mathrm{Tor}[O_{(S)}]}{\sqrt{\det V}} \tag{S17}$$

where

$$\mathrm{Tor}(A) = \sum_{Z \in P([N])} (-1)^{|Z|} \frac{1}{\sqrt{\det[1 - A_{(Z)}]}} \tag{S18}$$

in which O is a matrix derived from the covariance matrix

$$O = 1 - V^{-1} \tag{S19}$$

the subscript (S) of O means a submatrix by indexing elements of the detection outcome S, $P([N])$ is the power set of set $[N] = \{1, 2, \cdots, N\}$, and $|Z|$ denotes the cardinality of the set. This summation is over 2^N determinants, so it has the time complexity of $O(N^3 2^N)$.

In our model, the threshold detection probability can be calculated by the modified Torontonian, mTor(O). Firstly notice that the probability of detecting a vacuum state $\Pi_0 = |0\rangle\langle 0|$ is the multiplication of the probability that detect the vacuum state in each independent mode, and $P(\Pi_1) = 1 - P(\Pi_0)$. Employing the phase space representation of the output states and an

inclusive-exclusive formula, the output probability can be written as

$$p(S) = \frac{\mathrm{mTor}[O_{1_{(S)}}, O_{2_{(S)}}, \cdots, O_{M_{(S)}}]}{\prod_{m=1}^{M} \sqrt{\det V_m}} \tag{S20}$$

where

$$\mathrm{mTor}(A_1, A_2, \cdots, A_M) := \sum_{Z \in P([N])} (-1)^{|Z|} \prod_{m=1}^{M} \frac{1}{\sqrt{\det[1 - A_{m_{(Z)}}]}} \tag{S21}$$

in which O_m is a matrix derived from the covariance matrix independently

$$O_m = 1 - V_m^{-1} \tag{S22}$$

We observe that this equation is a multiplication of M single modes, so the time complexity is multiplied by a factor M.

6 Matrix product state method

6.1 Decomposition of the output state of GBS

The matrix product state (MPS) method [3] begins by decomposing the covariance matrix $\boldsymbol{V}$ of the output Gaussian state into two components: $\boldsymbol{V} = \boldsymbol{V}_p + \boldsymbol{W}$. Here, $\boldsymbol{V}_p$ represents the covariance matrix of a pure Gaussian state, and $\boldsymbol{W}$ is a positive semidefinite matrix ($\boldsymbol{W} \succcurlyeq 0$). This decomposition is performed using semidefinite programming (SDP) under specified constraints

$$\min_{\boldsymbol{V}_p} \mathrm{Tr}[\boldsymbol{V}_p] \text{ with } \boldsymbol{V} - \boldsymbol{V}_p \succcurlyeq 0, \boldsymbol{V}_p \succcurlyeq i \begin{pmatrix} 0 & 1 \\ -1 & 0 \end{pmatrix} \otimes \mathbf{1}_m, \tag{S23}$$

where m is the number of output modes.

To address this problem, we consider methods such as interior-point and first-order approaches. However, computational constraints, such as several hours and 128 GB of memory on a personal computer, limit the problem size. Interior-point methods are significantly slower than first-order methods for large-scale problems, and most first-order SDP solvers lack MPI support, rendering them unsuitable for supercomputer clusters. We employ the SCS solver [4] with the parameter use_indirect=True for $m < 2000$. For $m > 2000$, an analytical method is used, as described below.

6.1.1 Analytic method to decompose the output state

We denote the transformation matrix as $\boldsymbol{M}$ and the squeezing parameter as $\vec{r}$. The covariance matrix of the output state of GBS is

$$\boldsymbol{V} = \boldsymbol{T}\,\mathrm{Diag}(\mathrm{e}^{2\vec{r}}, \mathrm{e}^{-2\vec{r}})\boldsymbol{T}^T + \boldsymbol{I} - \boldsymbol{T}\boldsymbol{T}^T,$$

where

$$\boldsymbol{T} = \begin{pmatrix} \mathrm{Real}(\boldsymbol{M}) & -\mathrm{Imag}(\boldsymbol{M}) \\ \mathrm{Imag}(\boldsymbol{M}) & \mathrm{Real}(\boldsymbol{M}) \end{pmatrix}.$$

If $\boldsymbol{M}$ can be written as $\boldsymbol{M} = \boldsymbol{U}\,\mathrm{Diag}(\sqrt{\vec{\eta}})$, where $\boldsymbol{U}$ is a unitary matrix, $\boldsymbol{U}\boldsymbol{U}^\dagger = \boldsymbol{I}$, and $\vec{\eta}$ is the transmittance of the output entries, we can get

$$\boldsymbol{T} = \begin{pmatrix} \mathrm{Real}(\boldsymbol{U}) & -\mathrm{Imag}(\boldsymbol{U}) \\ \mathrm{Imag}(\boldsymbol{U}) & \mathrm{Real}(\boldsymbol{U}) \end{pmatrix} \mathrm{Diag}(\sqrt{\vec{\eta}}, \sqrt{\vec{\eta}}).$$

Define $\boldsymbol{A}$ as

$$\boldsymbol{A} = \begin{pmatrix} \mathrm{Real}(\boldsymbol{U}) & -\mathrm{Imag}(\boldsymbol{U}) \\ \mathrm{Imag}(\boldsymbol{U}) & \mathrm{Real}(\boldsymbol{U}) \end{pmatrix}.$$

Then $\boldsymbol{T}$ can be rewritten as

$$\boldsymbol{T} = \boldsymbol{A}\,\mathrm{Diag}(\sqrt{\vec{\eta}}, \sqrt{\vec{\eta}})$$

The covariance matrix of the output state is

$$\boldsymbol{V} = \boldsymbol{A}\,\mathrm{Diag}(\vec{\eta}\mathrm{e}^{2\vec{r}} + 1 - \vec{\eta}, \vec{\eta}\mathrm{e}^{-2\vec{r}} + 1 - \vec{\eta})\boldsymbol{A}^T.$$

So the pure state part of the output state is

$$\boldsymbol{V}_p = \boldsymbol{A}\,\mathrm{Diag}(\mathrm{e}^{2\vec{s}}, \mathrm{e}^{-2\vec{s}})\boldsymbol{A}^T,$$

where

$$\mathrm{e}^{-2\vec{s}} = \vec{\eta}\mathrm{e}^{-2\vec{r}} + 1 - \vec{\eta}.$$

$\vec{s}$ and $\boldsymbol{U}$ can be easily calculated from $\boldsymbol{M}$. However, generally the constraint $\boldsymbol{U}\boldsymbol{U}^\dagger = \boldsymbol{I}$ is not strictly satisfied. So we first use $\boldsymbol{U}$ and $\vec{s}$ to calculate $\boldsymbol{V'}$ and then perform the Williamson decomposition on $\boldsymbol{V'}$ to get $\boldsymbol{D}, \boldsymbol{S}$. Note that $\boldsymbol{D} = \boldsymbol{I}$ if $\boldsymbol{V'}$ is a pure state. For $\boldsymbol{V'}$ of experimental result, $\boldsymbol{D} \approx \boldsymbol{I}$. It means that $\boldsymbol{V'}$ is not a pure state while $\boldsymbol{V}_p = \boldsymbol{S}\boldsymbol{S}^T$ is a pure state, and $\boldsymbol{V}_p$ is a rather good

approximation for the target state. Nevertheless, $\boldsymbol{V}_p = \boldsymbol{S}\boldsymbol{S}^T$ may not satisfy the constraint S23, so we need to scale and search $\vec{s}$ globally to make $\boldsymbol{V}_p$ satisfy it. The algorithm is shown in Alg.1.

Algorithm 1: The analytic method to decompose the output state of GBS.

Data: $\vec{r}$,$\boldsymbol{T}$

Result: $\boldsymbol{V}_p$,$\boldsymbol{W}$

$\boldsymbol{V} = \boldsymbol{T}\,\mathrm{Diag}(\mathrm{e}^{2\vec{r}}, \mathrm{e}^{-2\vec{r}})\boldsymbol{T}^T + \boldsymbol{I} - \boldsymbol{T}\boldsymbol{T}^T$;

$\vec{\eta} = \mathrm{Diag}(\boldsymbol{T}^\dagger\boldsymbol{T})$;

$\vec{s} = -\ln(\vec{\eta}\mathrm{e}^{-2\vec{r}} + 1 - \vec{\eta})/2$;

$\boldsymbol{U} = \boldsymbol{T}/\sqrt{\vec{\eta}}$;

$\boldsymbol{V'} = \boldsymbol{U}\,\mathrm{Diag}(\mathrm{e}^{2\vec{s}}, \mathrm{e}^{-2\vec{s}})\boldsymbol{U}^T + \boldsymbol{I} - \boldsymbol{U}\boldsymbol{U}^T$;

$\boldsymbol{D}, \boldsymbol{S} = \mathrm{Williamson}(\boldsymbol{V'})$;

$\boldsymbol{V}_p = \boldsymbol{S}\boldsymbol{S}^T$;

$\boldsymbol{W} = \boldsymbol{V} - \boldsymbol{V}_p$;

while $\boldsymbol{W} \not\succcurlyeq 0$ *is not satisfied* **do**

  scale $\vec{s}$, $\vec{s} = \vec{s} \times 1.01$ for example;

  $\boldsymbol{V'} = \boldsymbol{U}\,\mathrm{Diag}(\mathrm{e}^{2\vec{s}}, \mathrm{e}^{-2\vec{s}})\boldsymbol{U}^T + \boldsymbol{I} - \boldsymbol{U}\boldsymbol{U}^T$;

  $\boldsymbol{D}, \boldsymbol{S} = \mathrm{Williamson}(\boldsymbol{V'})$;

  $\boldsymbol{V}_p = \boldsymbol{S}\boldsymbol{S}^T$;

  $\boldsymbol{W} = \boldsymbol{V} - \boldsymbol{V}_p$;

end

return $\boldsymbol{V}_p$,$\boldsymbol{W}$;

6.2 Estimate the lower bound of required bond dimension size to simulate the experiments

The high memory cost of processing large tensors precludes direct evaluation of the truncation error for the large bond dimensions required to simulate our experiments. Instead, we estimate the necessary bond dimension by extrapolating from data obtained at tractable parameter scales, analyzing the relationship between the truncation error ε and the bond dimension χ. .

First, we need to determine the function form to fit the calculable data points and perform the extrapolation. In [3], it shows that for a fixed-size circuit, the bond dimension scales as $\chi =$

$O(\text{polylog}(1/\epsilon))$ in the TVD ϵ. Here we consider the single-term polynomial hypotheses:

$$\chi = Ax^n \tag{S24}$$

where

$$x = \frac{\ln(1/\varepsilon)}{\ln(1/\varepsilon)_{\max}}$$

Here $\ln(1/\varepsilon)_{\max}$ is the max $\ln(1/\varepsilon)$ among the obtained data points and it is introduced for normalize and better fitting performance. We also considered other more complicated polynomial models which were found to be not numerically stable to fit the data points, so the simplest single-term model was chosen.

The fitting results are shown in Fig.S18.

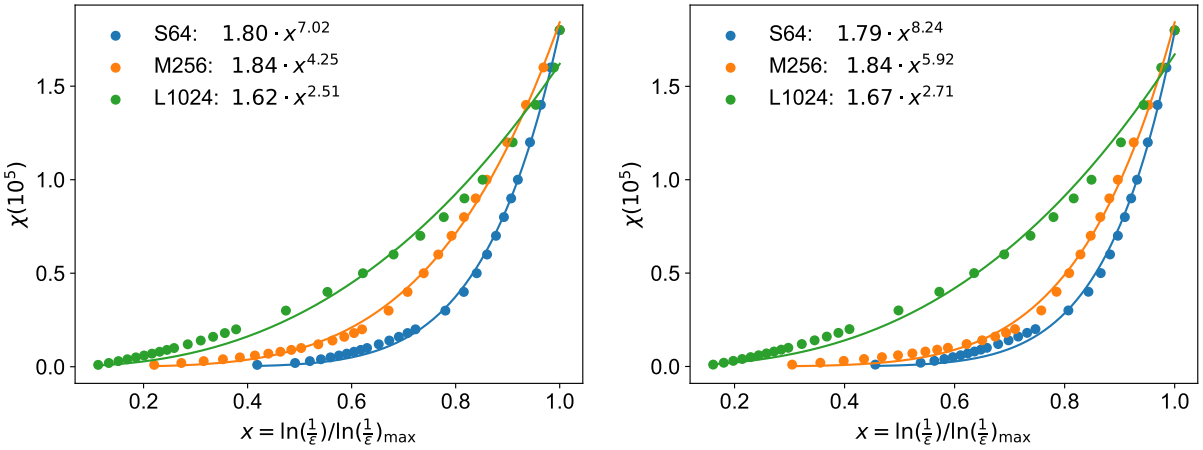

(a) dataset (6nJ)

(b) dataset (2nJ)

Figure S18: Fitted relation between the bond dimension χ and the truncation error ε.

We choose the truncation error $\varepsilon = 0.05$ as the target value to determine the needed size of bond dimension, the results are listed in Table S1.

Then we prove that we do get the lower bound from the extrapolation method, i.e. we do not over estimate the complexity. To verify this, we pick out the last several data points from the fitting set to serve as the validation set, and then perform the fitting and extrapolation using the left data points. As shown in Fig.S19, the extrapolated value of bond dimension is clearly smaller than the real value, which indicates that our procedure here indeed gives the lower bound of the needed size of bond dimension.

Data set	$\ln(1/\varepsilon)_{\max}$	χ	$A(10^5)$	n
S64 (6nJ)	2.68	3.88×10^5	1.80	7.02
M256 (6nJ)	5.06×10^{-2}	6.29×10^{12}	1.84	4.25
L1024 (6nJ)	6.87×10^{-7}	7.98×10^{21}	1.62	2.51
S64 (2nJ)	4.01	1.64×10^4	1.79	8.24
M256 (2nJ)	2.50×10^{-1}	4.56×10^{11}	1.84	5.92
L1024 (2nJ)	2.95×10^{-4}	1.12×10^{16}	1.67	2.71

Table S1: The bond dimension χ at target truncation error $\varepsilon = 0.05$ and the fitting parameters for different dataset. Note that $\ln(1/0.05) = 2.996$, most χs are the result of extrapolation and they are mainly determined by the leading term.

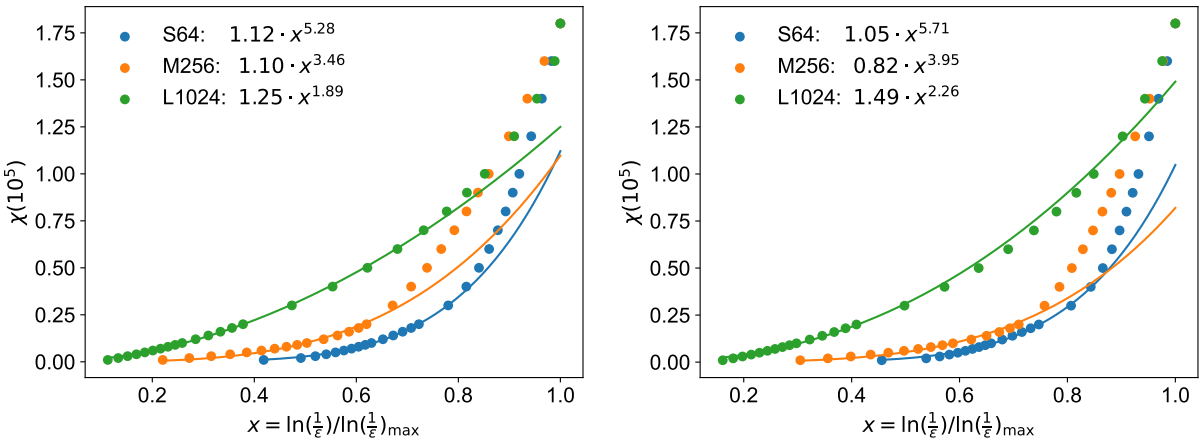

(a) dataset (6nJ)

(b) dataset (2nJ)

Figure S19: The relation between bond dimension χ and truncation error ε. The points are the data we used to fit and the lines are the fitting result of the model EQ(S24) for only the first 16 points.

6.3 Running time on the supercomputer

The complexity of MPS construction is given by

$$T_{\text{MPS}} = O(Md\chi^2 2^{\frac{N_{\text{eff}}}{2}}) \tag{S25}$$

To estimate the needed cost to simulate the experiments on the supercomputer, we first record the running time under moderate parameter level [5] and directly scale the needed cost for huge

Data set	S64 (6nJ)	M256 (6nJ)	L1024 (6nJ)	S64 (2nJ)	M256 (2nJ)	L1024 (2nJ)
M	4336	5104	8176	4336	5104	8176
χ	3.88×10^5	6.29×10^{12}	7.98×10^{21}	1.64×10^4	4.56×10^{11}	1.12×10^{16}
N_{eff}	6.92	27.69	113.54	4.47	18.02	74.19
T	4.44 s	5.82×10^{10} y	1.26×10^{42} y	3.40 ms	1.07×10^7 y	2.95×10^{24} y

Table S2: The time needed by El Capitan without hard disk IO for different dataset. M is the mode number, χ is the bond dimension, N_{eff} is the effective photon number and T is the time needed by El Capitan. The time is calculated using the bond dimension χ at target truncation error $\varepsilon = 0.05$. Local Hilbert space dimension d is set as 3.

parameter size based on the complexity shown above, which implicitly assumes unlimited memory. We only consider the computational cost of MPS construction, though the sampling cost is also massive under large bond dimension.

The dataset of M256 (2nJ) is used as the estimation base of moderate parameter size, with bond dimension $\chi_0 = 10000$, effective squeeze photon number $N_{\text{eff}_0} = 19.16$, mode number $M_0 = 5104$, dimension of a local Hilbert space $d_0 = 3$. The running time on an Nvidia A100 is 6 hours if only the float point operation time is included and no hard disk IO time is considered. The FP32 performance of A100 is 19.5 TFLOPS, and the Rmax of the fastest supercomputer El Capitan is 1.742 EFLOPS, so we can figure out that the time needed by El Capitan is $t_0 = \frac{19.5\times3600\times6}{1.742\times10^6} = 0.2418$ s.

The complexity of obtaining all the matrix elements for MPS is $O(Md\chi^2 \times$ (hafnian of $\sum n_1, n_2$)). Here we replace hafnian of $\sum n_1, n_2$ with the $2^{N_{\text{eff}}/2}$, N_{eff} is the effective squeeze photon number. So the time needed by El Capitan is

$$t = t_0 \times \frac{Md\chi^2 2^{N_{\text{eff}}/2}}{M_0 d_0 \chi_0^2 2^{N_{\text{eff}_0}/2}} \tag{S26}$$

The time needed by El Capitan for different data sets are shown in Table S2.

It is worth noting that the actual squeeze photon number of data set M256(2nJ) in the table is a little different from that we used as reference, because when do the decomposition that $V = V_p + W$, we scale $\vec{s}$ a little to make V_p satisfy the constraint S23. So the actual squeeze photon number used to do the real MPS decomposition will be a little larger than the one we used to calculate the time.

It means that the time needed by supercomputer is a little larger than the one we calculated, which ensure the time we give is a lower bound.

References and Notes

[1] N. Quesada, J. E. Sipe, Effects of time ordering in quantum nonlinear optics. *Physical Review A* **90** (6), 063840 (2014), doi:10.1103/PhysRevA.90.063840, https://link.aps.org/doi/10.1103/PhysRevA.90.063840.

[2] N. Quesada, G. Triginer, M. D. Vidrighin, J. E. Sipe, Theory of high-gain twin-beam generation in waveguides: From Maxwell's equations to efficient simulation. *Physical Review A* **102** (3), 033519 (2020), doi:10.1103/PhysRevA.102.033519, https://link.aps.org/doi/10.1103/PhysRevA.102.033519.

[3] C. Oh, M. Liu, Y. Alexeev, B. Fefferman, L. Jiang, Classical Algorithm for Simulating Experimental Gaussian Boson Sampling pp. 1–8, doi:10.1038/s41567-024-02535-8, https://www.nature.com/articles/s41567-024-02535-8.

[4] B. O'Donoghue, Operator Splitting for a Homogeneous Embedding of the Linear Complementarity Problem. *SIAM Journal on Optimization* **31**, 1999–2023 (2021).

[5] Y. Chen, *et al.*, FastMPS: Breaking the Scaling Barrier of MPS-based Gaussian Boson Sampling Simulation.